Journal of Applied Geophysics 251 (2026) 106231

Contents lists available at ScienceDirect

Journal of Applied Geophysics

journal homepage: www.elsevier.com/locate/jappgeo

On the detectability of local, high-velocity anomalies in acoustic crosshole full-waveform inversion

Sarah Beraus [a,b,*], Daniel Köhn [c], Thomas Bohlen [d], Thomas Burschil [e], Hermann Buness [a], Gerald Gabriel [a,b]

[a] Geophysical Exploration, LIAG Institute for Applied Geophysics, Stilleweg 2, 30655 Hannover, Lower Saxony, Germany
[b] Section Geology, Institute of Earth System Sciences, Leibniz University Hannover, Callinstraße 30, 30167 Hannover, Lower Saxony, Germany
[c] Institute of Geosciences, Kiel University, Otto-Hahn-Platz 1, 24118 Kiel, Schleswig-Holstein, Germany
[d] Geophysical Institute, Karlsruhe Institute of Technology, Hertzstraße 16, 76187 Kalrsruhe, Baden-Württemberg, Germany
[e] B3.2, Federal Institute for Geosciences and Natural Resources, Stilleweg 2, 30655, Hannover, Lower Saxony, Germany

ARTICLE INFO

Dataset link: https://doi.org/10.5880/ICDP.5068.002

Keywords:
Full-waveform inversion
Anisotropic smoothness constraints
Acoustic
Crosshole
Glacial sediments

ABSTRACT

In this study, two-dimensional, time-domain full-waveform inversion (FWI) is applied to crosshole seismic data acquired in the glacially overdeepened Tannwald Basin (ICDP site 5068_1), located north of Lake Constance, to derive a high-resolution P-wave velocity model. The acoustic waves were excited by a sparker source in borehole B and recorded by a 24-station hydrophone string in borehole C, 28 m away. Data preprocessing included extensive tube wave suppression using fk-filtering. Existing traveltime tomography models were used as initial models for the acoustic waveform inversion. Although the two applied workflows yield very similar waveform fits and final misfit values, their outcomes differ: the run using an anisotropic gradient smoothing filter produces a background model with a high vertical resolution, while the isotropic gradient smoothing results in the inversion of local high-velocity anomalies that introduce X-shaped artifacts. A comparison with sonic logs confirms that both models significantly improve the initial model, but also display discrepancies beyond the sonic logs' error range. We conclude (1) that gradient smoothing is a critical parameter in FWI and should be thoroughly tested, especially when FWI including uncertainty quantification cannot be performed, and (2) that two extremal smoothing realizations facilitate to infer a comprehensive conceptual geological interpretation.

1. Introduction

The idea of full-waveform inversion (FWI) was first formulated by Tarantola (1984). Unlike traveltime tomography, which relies solely on traveltime picks, FWI uses the entire waveform, to obtain high-resolution subsurface models. It has been applied to a range of scales from ultra-high-resolution medical imaging (Kühn, 2018), via near-surface seismics (Mecking et al., 2021) and deep reflection seismics (Virieux and Operto, 2009; Warner et al., 2013), to seismology (Tromp, 2020).

Nevertheless, field data application remains challenging due to, i.a., many choices in the FWI setup including the selection of a proper initial model, data pre-conditioning, and the optimization of workflow parameters. While the community is aware of these challenges, comparative studies examining the influence of these choices are not well documented.

Since the crosshole geometry offers an excellent illumination, it is frequently used in synthetic tests aimed to advance methodological developments, such as the validation of the multi-scale approach in the frequency domain (Pratt and Shipp, 1999), the medium parameterization and crosstalk tests (Barnes et al., 2008; Hadden and Pratt, 2017; Hadden et al., 2019), and examining gradient smoothing (Hadden and Pratt, 2017).

Field data applications of acoustic FWI show its versatility. For instance, laboratory experiments by Zhou et al. (1997) aimed to establish frequency-domain visco-acoustic FWI using an epoxy resin model, while well-log constraints were incorporated by Wang and Rao (2006) to guide the inversion. Moreover, acoustic FWI has become a tool for monitoring reservoirs or CO_2 injection sites in time-lapse experiments (Zhang et al., 2012), with modern machine learning approaches also being employed (Yang et al., 2024). A case study in gas-hydrate-bearing

* Corresponding author at: Section Geology, Institute of Earth System Sciences, Leibniz University Hannover, Callinstraße 30, 30167 Hannover, Lower Saxony, Germany.
E-mail address: Sarah.Beraus@liag-institut.de (S. Beraus).

https://doi.org/10.1016/j.jappgeo.2026.106231
Received 27 May 2025; Received in revised form 23 January 2026; Accepted 25 March 2026
Available online 25 April 2026

sediments by Pratt et al. (2005) showcased the method's ability to produce high-resolution images of the subsurface.

In this study, we apply isotropic, acoustic, time-domain FWI (Köhn et al., 2012) to seismic crosshole data acquired in the sediments of the glacially overdeepened Tannwald Basin in southern Germany. This basin is investigated in the context of landscape evolution within the "Drilling Overdeepened Alpine Valleys" (DOVE) project of the International Continental Scientific Drilling Program (ICDP). We evaluate how two different workflow designs influence the inverted velocity model, highlighting the data's inherent ambiguity, and assess which approach is better suited for identifying sequences or anomalies, as well as present a comprehensive conceptual geological model derived from the velocity models and the existing interpretation of the core of one of the boreholes (Schuster et al., 2024).

2. Theory of 2D acoustic full waveform inversion

Full-waveform inversion (FWI) takes into account both the phase and amplitude information of seismic waves which allows to derive information on the material properties of the subsurface below the dominant seismic wavelength (Virieux and Operto, 2009). In this study, we use the open source software DENISE-Black-Edition which is available under https://github.com/daniel-koehn/DENISE-Black-Edition (Köhn, 2025b).

2.1. 2D acoustic equations of motion

We apply time-domain finite-difference (FD) modeling to numerically solve the 2D isotropic acoustic equations of motion (Alford et al., 1974), describing the propagation of P-waves, on a staggered grid (Yee, 1966). In the stress-velocity formulation, these equations are given in the form of a system of first-order partial differential equations as

$$\begin{aligned} \rho \frac{\partial v_x}{\partial t} &= \frac{\partial p}{\partial x} \\ \rho \frac{\partial v_z}{\partial t} &= \frac{\partial p}{\partial z} + f \\ \frac{\partial p}{\partial t} &= \lambda \left(\frac{\partial v_x}{\partial x} + \frac{\partial v_z}{\partial z} \right), \end{aligned} \tag{1}$$

where x and z are the horizontal and vertical coordinates, respectively; t is the time, ρ is the density, and λ is the first Lamé parameter. The particle velocities are denoted by v_i, where the index i indicates the respective direction, and pressure as p; f represents the source term.

2.2. 2D P-wave FWI strategy

In an iterative approach FWI minimizes the misfit between the field and the modeled data to obtain the optimal model of the subsurface. The initial model parameters $\mathbf{m}_0$ are updated to $\mathbf{m}_n$ at each inversion step n along a search direction $\delta\mathbf{m}_n$ by

$$\mathbf{m}_{n+1} = \mathbf{m}_n + \alpha_n \, \delta\mathbf{m}_n, \tag{2}$$

where α_n is the step length. It is determined in a parabolic line search to ensure proper convergence (Nocedal and Wright, 2006). The model update at inversion step n is defined by

$$\delta\mathbf{m}_n = -H_n^{-1} \left(\frac{\partial E}{\partial \mathbf{m}} \right)_n . \tag{3}$$

Here, H^{-1} is the inverse Hessian matrix, which is approximated at each iteration by the time-integrated squared absolute value of the forward wavefield (Zhang et al., 2012), and $\partial E/\partial \mathbf{m}$ is the gradient of the misfit function.

Since acoustic FWI cannot properly reconstruct the amplitude dynamics (Hadden et al., 2019), the global correlation norm (GCN) is chosen as misfit function. It is given by

$$E = -\sum_{i=1}^{ns} \int_0^T \mathrm{d}t \sum_{j=1}^{nr} \left[\frac{u_{ij}^{\mathrm{mod}}(t)\, u_{ij}^{\mathrm{obs}}(t)}{\|u_{ij}^{\mathrm{mod}}(t)\|_2 \, \|u_{ij}^{\mathrm{obs}}(t)\|_2} \right], \tag{4}$$

where ns and nr are the number of sources and receivers, and T is the recording time. The modeled and observed data are denoted as u_{ij}^{mod} and u_{ij}^{obs}, respectively, and $\|\cdot\|_2$ is their L2-norm. By using the trace-normalized data, the GCN misfit function reduces the sensitivity to amplitude errors and effectively gives the phase information a higher weight (Choi and Alkhalifah, 2012).

The gradient of the misfit function is calculated with the adjoint-state method via zero-lag cross-correlation between the forward modeled and the adjoint wavefields using the stress-velocity parameterization (Köhn et al., 2012). By employing a strict Nyquist criterion given by

$$DT_{\mathrm{samp}} \leq \frac{1}{8 \cdot f_{\mathrm{max}}}, \tag{5}$$

where f_{max} is the maximum frequency at the current inversion stage and DT_{samp} the time sampling interval at which the wavefield has to be saved to accurately apply the imaging condition, we reduce RAM usage (Kurzmann, 2012). For the parameters used in this study, this yields a reduction by a factor of seven for the initial inversion tests up to 800 Hz, whereas for the frequency range from 100 to 500 Hz (see Table 1), the reduction could have been as large as a factor of twelve.

The computational cost required to calculate the inverse Hessian is circumvented by approximating it by a preconditioning operator (Nocedal and Wright, 2006). To increase the convergence speed, we additionally use a weighting factor defined by Polak and Ribiere (1969).

Furthermore, we apply the multi-stage approach (Bunks et al., 1995) as given in Table 1 in order to treat the non-linearity of the inversion problem. We filter the data at each inversion stage with a sixth-order zero-phase bandpass filter with a lower corner frequency of 100 Hz (see Table 1), apply the source-time function (STF) inversion at the first iteration of each new frequency stage, and run at least 20 iterations per frequency stage. We omit the 100–450 Hz frequency stage to reduce the computational cost. This decision is justified by the observation that no cycle skipping occurs when increasing the maximum frequency from 400–500 Hz, suggesting that the inversion remains in the current minimum of the misfit function and does not transition to an alternative minimum.

We also apply a Gaussian filter to smooth the gradient and eliminate short-wavelength artifacts (Ravaut et al., 2004). The filter length is defined based on a fraction (γ_{x_i}) of the minimum P-wave wavelength, given by

$$\gamma_{\mathrm{gauss,x_i}} = \gamma_{x_i} \frac{v_{\mathrm{P,mean}}}{f_{\mathrm{max}}}, \tag{6}$$

where x_i refers to the spatial coordinate x or z. This results in a spatially varying filtering effect that is adapted to the local velocity model.

As outlined in Table 1, two workflows are examined, implicitly illustrating the impact of the gradient filter on the resulting velocity models. They differ with regard to the gradient smoothing. Workflow W1 uses anisotropic smoothing with a greater horizontal than vertical correlation length ($\gamma_x > \gamma_z$) in the higher frequency stages. Workflow W2 uses isotropic smoothing, where the horizontal correlation length (γ_x) matches the vertical correlation length (γ_z). Furthermore, W1 uses strong smoothing in the initial frequency stages to obtain a smooth background model ensuring convergence in the initial stages. With the experience of the FWI using W1 (and further tests) and the intend to focus on local velocity anomalies, W2 uses a filter length corresponding to the local minimum wavelength to retain the highest possible resolution. The choice of smoothing parameters is further guided by the acquisition geometry and prior geological knowledge, such as the existence of sand lenses and larger components in the diamict as inferred from core analysis (Schuster et al., 2024).

In addition, a cylindrical taper is applied at each shot position to smooth extremal updates at these positions.

We define three abort criteria: (a) a relative misfit change of less than 1%, (b) a failed line search after six attempts, and (c) a maximum number of total iterations of 600. The inversion stops when any one of the criteria is met.

Table 1
Tested FWI workflows (W1 and W2). All frequency stages start at 100 Hz. The Gaussian gradient smoothing filter is defined by the horizontal (γ_x) and vertical (γ_z) filter lengths that are defined by a fraction of the mean wavelength at the respective stage. In case of γ_x being larger than γ_z the Gaussian filter is anisotropic (W1), in case of γ_x is the same as γ_z the Gaussian filter is isotropic (W2). The 100–450 Hz frequency stage is omitted to reduce the computational cost.

Stage	f_{min} in Hz	f_{max} in Hz	W1		W2	
			γ_x	γ_z	γ_x	γ_z
1	100	150	2.0	2.0	1.0	1.0
2	100	200	2.0	2.0	1.0	1.0
3	100	250	2.0	2.0	1.0	1.0
4	100	300	2.5	0.5	1.0	1.0
5	100	350	2.5	0.5	1.0	1.0
6	100	400	2.5	0.5	1.0	1.0
7	100	500	2.5	0.5	1.0	1.0

3. Study site: Tannwald Basin (ICDP site 5068_1)

Our study site (ICDP site 5068_1) is located approximately 45 km north of Lake Constance in the glacially overdeepened Tannwald Basin (Fig. 1). Overdeepened valleys are elongated structures carved into the bedrock by glaciers below the fluvial base level, which were subsequently refilled, often multiple times, with rocks and sediments transported by the glacial system (Cook and Swift, 2012). After the Alpine Rhine established its current course in the Early Pleistocene (Ellwanger et al., 2003), at least two glacial cycles contributed to the formation of the overdeepened north–south trending Tannwald Basin in the Quaternary (Ellwanger et al., 2011; Preusser et al., 2010). During the Hosskirch glaciation, a Rhine Glacier lobe incised into the bedrock of Tertiary Upper Freshwater Molasse and the underlying Upper Marine Molasse at the basin's deepest part, forming the D3 discontinuity (Ellwanger et al., 2011), as shown in Fig. 1. Today, the Tannwald Basin is a distal overdeepened structure, roughly 1 km wide and up to 250 m deep. Its infill consists of waterlain till and molasse slabs, which were deposited during the Hosskirch glaciation, which appear as strong, seismic reflectors (Burschil et al., 2018). Overlying these are basinal, fine-grained sediments that accumulated in a large glacial lake as laminated fines until the Early Rissian. The transition to coarse-grained clastics interspersed with till layers, known as the D2 discontinuity (Fig. 1), marks the advance of a glacier lobe during the Riss glaciation. The uppermost layer consists of glaciofluvial gravels from the outwash plane of the Last Glacial Maximum (LGM), with a thickness of about 10 m (Buness et al., 2022), indicating another glacial advance that almost reached the site.

The drill site lies just beyond the terminal moraine of the LGM (Fig. 1); so the youngest D1 discontinuity is absent. Three boreholes were drilled down to the bedrock at about 160 m depth at the site: two flush drillings (A and B), and one cored drilling (C). The boreholes are arranged in an isosceles triangle, with edges measuring 28 m in the north–south (AB) and west–east (BC) directions. During the flush drilling of borehole B, a coarse lithology was obtained from cuttings (DOVE-Phase 1 Scientific Team et al., 2023c,b,a). However, the sand was probably flushed out and could not be distinguished from the drilling mud. Schuster et al. (2024) derived seven lithofacies assemblages (LFA) with a high precision based on sedimentary characteristics found in the core of borehole C and linked them to the glacial history of the overdeepened valley. In addition, wireline logging data was acquired including sonic logs (DOVE-Phase 1 Scientific Team et al., 2023a).

4. Data acquisition

4.1. Crosshole seismic measurements

The sparker crosshole experiment was one of three crosshole tests conducted at the ICDP DOVE Tannwald site (5068_1) in 2022 (Beraus et al., 2024b). The dense transmission geometry effectively bypasses the attenuating weathering layer, preserving high-frequency information. A sparker borehole source was triggered eight times every meter between 37 and 146 m depth in borehole B (Fig. 2). We recorded the wavefield with a 24-station hydrophone string with a pre-set pre-amplification factor of 4, spaced 2 m apart, at depths ranging from 28 to 162 m in borehole C and a sampling frequency of 1 kHz. The desired depth coverage, shown in Fig. 2, was reached, and the receiver spacing was reduced to 1 m by shifting the string five times, ensuring an overlap at at least one station.

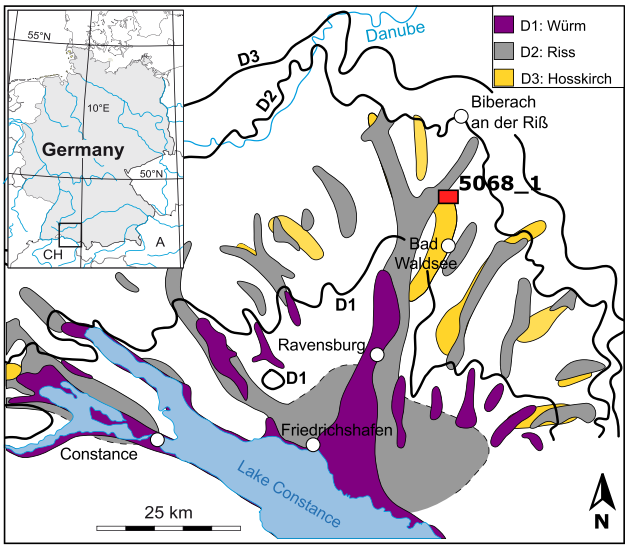

Fig. 1. Map of the overdeepenings of the Rhine Glacier in the Quaternary in the northern Alpine Foreland (modified after Ellwanger et al. (2011) and Beraus et al. (2024b)). The study site is marked by the red square. Black lines indicate the maximum ice extent during the corresponding glaciation period.

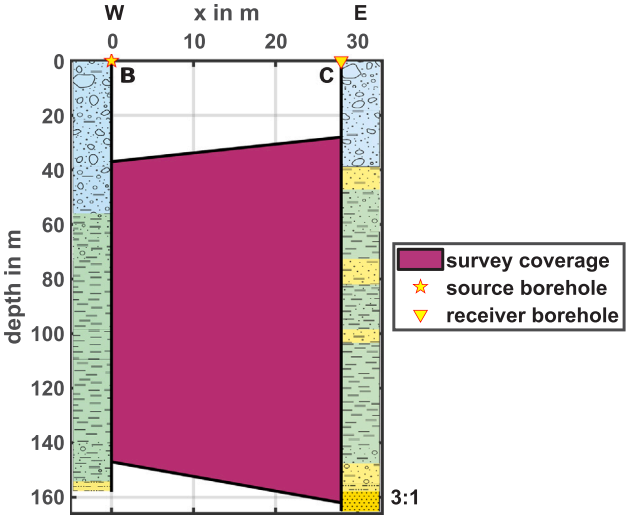

Fig. 2. Coverage of sparker data acquisition between boreholes B and C, and preliminary lithology based on cuttings (B) and core catcher information (C) (DOVE-Phase 1 Scientific Team et al., 2023c). Shots were made every meter between 37 and 146 m depth in borehole B. The wavefield was recorded with a 24-station hydrophone string at depths ranging from 28 to 162 m in borehole C, shifting the string to obtain a receiver spacing of 1 m.

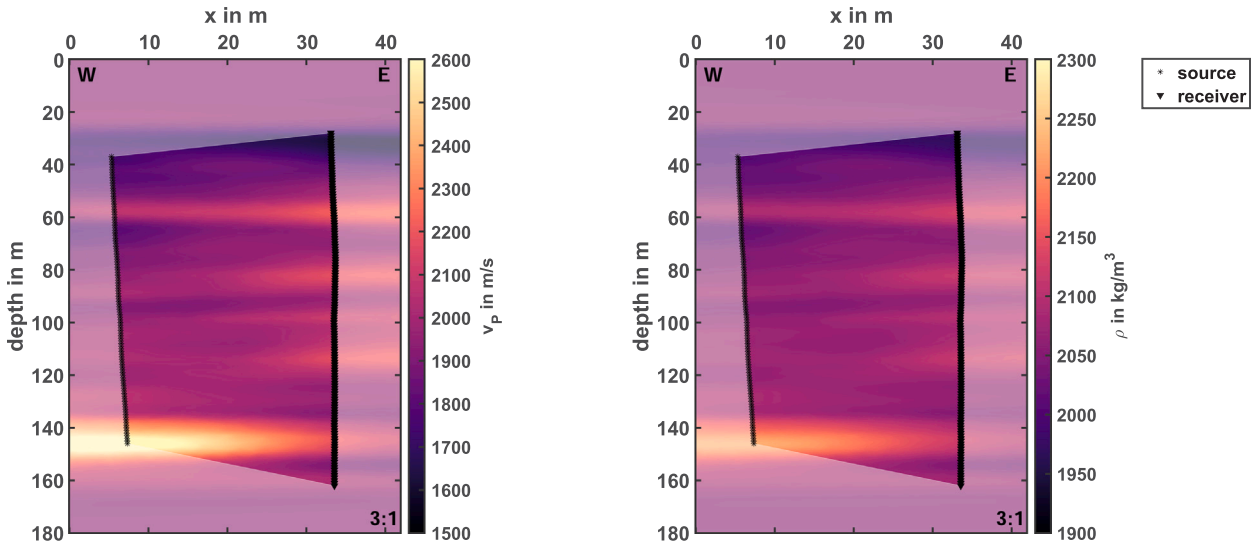

Fig. 3. Smoothed first arrival traveltime tomography model (Beraus et al., 2024b) and density model. The colormap used here and the colormaps used in subsequent figures follow Crameri (2023).

4.2. Sonic logging

In 2022, following the drilling campaign of 2021 and the installation of the PVC pipe casing, wireline logging was conducted in all three boreholes at site 5068_1 (DOVE-Phase 1 Scientific Team et al., 2023b,a; Schaller et al., 2025). For this study, the sonic log, which was recorded by a probe manufactured by ANTARES and provides the P-wave velocity in the vicinity of the borehole, is of particular interest. The sonic probe is equipped with two receivers (near and far) with a distance d of 0.5 m to mitigate the impact of the borehole diameter. Each of the receivers recorded a seismic trace every 0.1 m.

5. Preprocessing

5.1. Initial model building

Following the approach of Beraus et al. (2025), we first assign the geometry and vertically stack the repeated shots. Then, we pick the P-wave first arrivals. From these picks, an initial velocity model was obtained in a previous study by Beraus et al. (2024b) performing an isotropic traveltime tomography on a triangular mesh using the inversion code *pyGIMLi* (Rücker et al., 2017). The algorithm follows the damped Gauss–Newton method with global (Günther et al., 2006) and additional geostatistical regularization (Jordi et al., 2018). The traveltime inversion of P-wave picks yields a predominantly layered model due to the applied horizontal smoothing.

The model is re-interpolated and discretized on a Cartesian staggered grid with a grid spacing of 0.1 m to avoid numerical dispersion when using a sixth order FD operator in space with Taylor coefficients (Dablain, 1986; Levander, 1988). We also add 3 m-thick model boundaries on each side of the model to absorb artificial reflections at the model boundaries using an absorbing boundary zone in the form of a convolutional perfectly matched layer (CPML) (Komatitsch and Martin, 2007). This results in an FD grid of 1800×420 ($NZ \times NX$) grid points.

The density model is calculated based on this P-wave velocity model using a modified Gardner's equation (Gardner et al., 1974)

$$\rho = 310 \cdot v_{\mathrm{P}}^{0.25}, \tag{7}$$

where the density ρ is given in units of $\mathrm{kg\,m^{-3}}$ and the P-wave velocity v_{P} in $\mathrm{m\,s^{-1}}$. The initial models are further smoothed over 55 grid points using a Gaussian filter and are shown in Fig. 3.

5.2. Forward modeling

The wavefield is simulated based on the traveltime tomography and the density models. Based on the power spectrum of the data, which shows a significant decrease in the contribution of frequencies above 800 Hz due to the anti-aliasing filter (Fig. 4), we use a lowpass-filtered spike wavelet ($f \leq 800$ Hz). As source mechanism we choose an explosive pressure source. To fulfill the Courant–Friedrichs–Lewy stability criterion (Courant et al., 1967), we choose a temporal discretization of 0.02 ms with a second order FD operator in time.

5.3. Crosshole seismic data preprocessing

The data are contaminated by high-amplitude tube waves propagating through both the source and receiver well. Therefore, we apply fk-filters (Watanabe et al., 2005; Beraus et al., 2024b) in Shearwater's *Reveal* software that are defined as a polygon by dip (in ms/trace) and amplitude. The first filter is defined such that all events with velocities smaller than $1550\,\mathrm{m\,s^{-1}}$ are filtered out of the common receiver gathers (CRG); the second filter is less restrictive and filters out all events with velocities less than $1410\,\mathrm{m\,s^{-1}}$ from the common shot gathers (CSG). Further processing is done using the open-source code BIRGIT (Köhn, 2025a). We use the P-wave picks to apply a time-window that starts 5 ms before the pick and ends 20 ms after the pick, excluding an exponential taper with damping constant 10^5, to focus on the direct arrival. Using a 6th order zero-phase bandpass filter, we identify the frequency contribution below 100 Hz as noise. The cumulative power spectrum of the entire dataset (black) and three selected shot gathers (colored) are shown in Fig. 4.

Further, we mute the trigger peak at time zero. Next, a 3D-to-2D spreading correction (Bleistein, 1986) is applied to account for the amplitude and phase differences between the measured 3D and the simulated 2D wavefield (Forbriger et al., 2014; Schäfer et al., 2014). For this processing step, we choose a phase velocity of $2000\,\mathrm{m\,s^{-1}}$ and a maximum frequency of 1 kHz as parameters. In combination with the forward simulated synthetics, we perform a source-time function (STF) inversion that uses all traces per shot with a maximum offset of 101 m and determine the required damping parameter for the stabilized Wiener deconvolution, which is applied in the frequency domain, to be 1%. Here, we also find that a time delay of 0.025 s is necessary to obtain causal source wavelets. Finally, we apply a shot-wise normalization to the absolute maximum amplitude of each shot gather, minimizing the impact of the source energy variations that might occur due to an

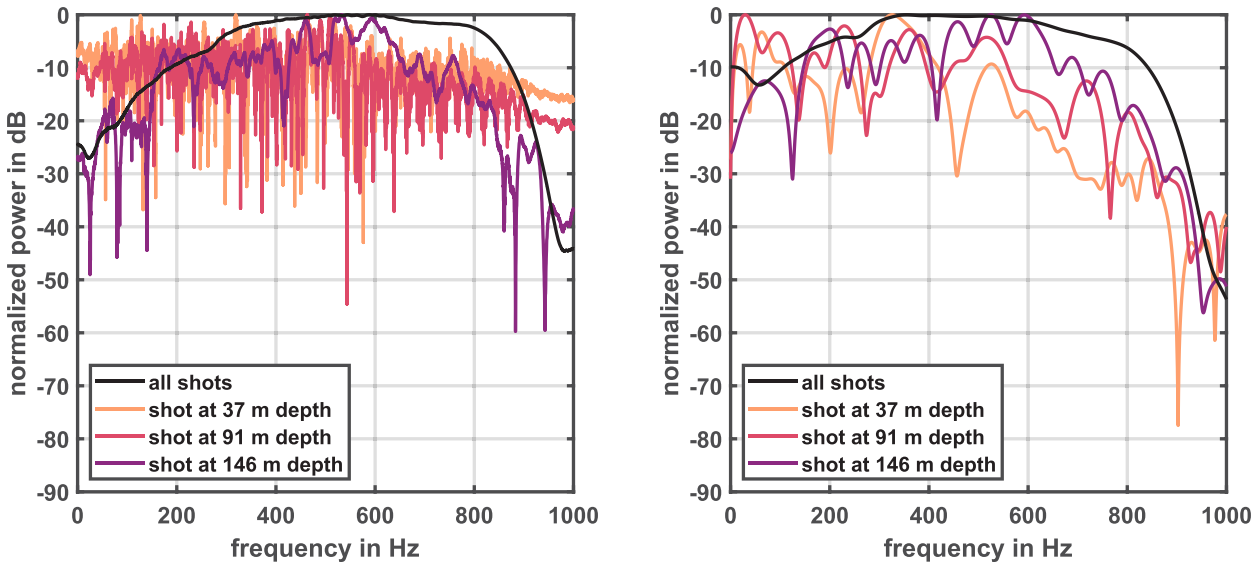

Fig. 4. Cumulative power spectrum of the raw data (left) and preprocessed data (right; long time-window) that was acquired with a sparker in borehole B and a 24-station hydrophone string in borehole C. The significant contributions below 100 Hz are related to noise and barely contain any signal. The colored curves refer to the shot depths presented in Fig. 5.

incompletely loaded impulse generator, on the amplitudes (Schwardt et al., 2020). In addition, we mute noisy traces and the overall noisy shots at 124 and 130 m depth.

Fig. 5 illustrates the initial waveform fit of the shallowest, an intermediate-depth and the deepest shot. Despite the removal of noisy traces, the inverted source wavelet of the first shot is less sharp than that of the other two presented shots.

5.4. Sonic data processing

According to DOVE-Phase 1 Scientific Team et al. (2023b), first, a depth correction using the spectral-gramma-ray (SGR) log is made. Next, to obtain the sonic velocities, the first arrivals recorded at the near and far traces are picked in WellCAD. The sonic velocity, denoted as v_{sonic}, is then calculated using

$$v_{\text{sonic}} = \frac{d}{t_{\text{far}} - t_{\text{near}}}, \tag{8}$$

where d is the receiver distance, and t_{far} and t_{near} are the picking times at the far and near receiver, respectively.

Since the actual vertical resolution of the sonic log is equal to the receiver distance, we smooth the log using a Gaussian filter with a length of 0.5 m.

In addition, the velocity error of the sonic logs is calculated. In this analysis, we assume that the distance d between the receivers is accurately known. Thus, the remaining errors are attributed to the measurement accuracy Δt_{a} and the picking accuracy Δt_{p}, which are assumed to be independent. The former is provided by the manufacturer to be $\pm 3\,\mu$s, and the latter is estimated to be $\pm 20\,\mu$s. Thus, the velocity error, Δv, is calculated from (8) using Gaussian error propagation as

$$\Delta v = v^2 \frac{\Delta t_{\text{a}} + \Delta t_{\text{p}}}{d}. \tag{9}$$

6. Results

6.1. Comparison of FWI workflows

The FWI results at frequency stage 7 (100–500 Hz), using the workflows described in Section 2.2 Table 1 and the data presented in Section 5, are displayed in Fig. 6. In general, the inversion enhances the velocity contrasts and thus the resolution of the subsurface model. The most significant features that are introduced by both FWI workflows are: An about 2.5 m thin high-velocity layer at about 35 m depth (a), just at the boundary of the area of maximum coverage. Furthermore, we see evidence of a depression (b) with an apex at 21 m along the x-coordinate and a depth of 123 m in the form of a high-velocity concave feature. Below 120 m depth on the receiver side in the east, alternating, low-velocity layers (c) are inverted. These layers also extend into the depth of the very high-velocity layer (d), which is almost continuous in the initial traveltime tomography model (d_0). Here, the high-velocity layer below 140 m depth is interrupted by two low-velocity layers (e), and an additional very low-velocity layer directly below (f). A similar but weaker and less vertically variable velocity reduction (g) is observed above the very high-velocity layer on the source side in the west. In addition, bending structures (h) are introduced above and below the source and receiver depths in the shaded areas and significant velocity updates are made in the western and eastern boundary zones (thickness of 3 m) of the model (i).

Workflow W1 mostly refines the traveltime tomography model and very closely resembles a horizontally layered medium, wherein the velocity differences are less pronounced than in the model obtained by workflow W2. Nevertheless, the depression feature (b) appears at around 120 m depth. Considering the model updates shown in Fig. 6 (top), we observe that the velocities tend to be increased in the center part of the illuminated area (j) and decreased close to the sources and receivers (g).

In contrast, workflow W2 introduces significant, steeply dipping high-velocity zones. In the shallow part, those form an almost X-shaped feature (k) with its center at 28 m along the x-coordinate and at 58 m depth, reaching a depth of about 90 m in the west. In the deeper part the diagonal high-velocity zone is tangential to the depression and dipping from east to west (l), where it almost touches the very high-velocity zone (d) below 140 m depth. Thus, the depression (b) boundary appears quite pronounced in the east, but it terminates in the west at a x-coordinate of 12 m as depicted in the plot of the FWI updates in Fig. 6.

Both FWI runs converge at stage 7 after 147 iterations (Fig. 7). The largest misfit reduction in workflow W1 of 5.2% is achieved at frequency stage 1 (100–150 Hz), followed by 4.2% at stage 4 (100–300 Hz) and 2.7% at stage 7 (100–500 Hz). The misfit of stages 2 (100–200 Hz)

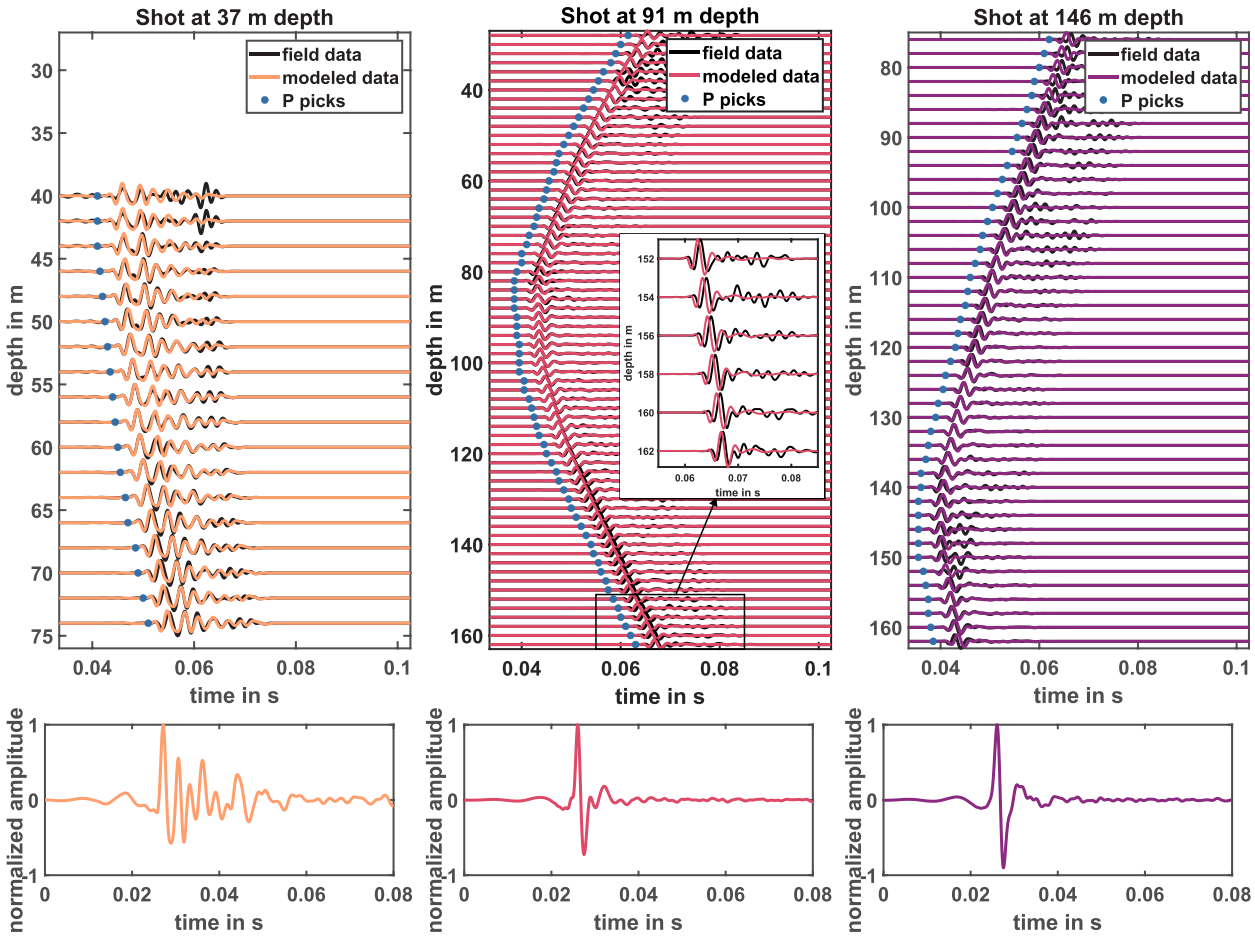

Fig. 5. Top: Comparison of forward modeled data based on the traveltime tomography models including STF inversion and the pre-processed and bandpass filtered (100–500 Hz) field data used in workflow W2. For better visualization, only every second trace is plotted, and an inset of the intermediate-depth shot presents an enlarged view of the deeper traces. The data misfit is smaller than half a period for most shots and traces. Bottom: Normalized wavelets obtained by source-time function (STF) inversion using the stabilized Wiener deconvolution.

and 3 (100–250 Hz) remains stagnant after more than 1% misfit reduction at the first iteration of both stages. Workflow W2 yields the biggest misfit reduction with 8.3% at stage 1 (100–150 Hz) and the second largest, of 3.0%, at stage 2 (100–200 Hz). Note that the data changes at every new frequency stage when higher frequencies are included. Overall, workflow W2 yields the lower final misfit value. While workflow W1 requires about four days of computing time on 320 CPUs (17.5 min/CPU), the FWI using workflow W2 finishes after about two days and 17 h on 320 CPUs (12 min/CPU), making workflow W2 computationally more efficient.[1]

The waveform fits of workflows W1 and W2 at stage 7 (100–500 Hz), where most of the small-scale structures are introduced into the model, are shown in Figs. 8 and 9, respectively. The shallowest shot shows the largest misfit, where the uppermost traces were muted due to their high noise level. This is still reflected in the inverted source wavelet, which has a long, high-amplitude coda. For the intermediate and deepest shot, the first arrival waveforms are well fitted. Reflection events included in the time-window, such as the event at just above 40 m depth, can also be explained by the inverted model compared to the initial model. The wavelets for these shots look very similar and are slightly mixed-phase with small precursors. The waveform fit obtained by workflow W2 (Fig. 9) is very similar to that of workflow W1; so are the wavelets.

[1] Note that the times per CPU also include MPI communication time.

6.2. Synthetic resolution test

To investigate the resolution capacity of the data and the FWI approaches, as well as to test the hypothesis that the steeply-dipping high-velocity zones that are inverted by workflow W2 are caused by high-velocity anomalies in the crosshole geometry, we put five circular high-velocities anomalies with a radius of 1.5 m into a background model given by the traveltime tomography model (Fig. 10 (left)). The high-velocity anomalies have velocities of 2800 m s^{-1}. In this FWI, we do not apply the STF inversion, since the wavelet is known from the simulation of the synthetic data.

Fig. 10 (center) shows the results at stage 7 (100–500 Hz), and Fig. 10 (right) depicts the difference between the initial tomography model and the respective FWI models. Despite the circular shape of the anomalies, the reconstruction shows sharp horizontal upper and lower boundaries (↑: lower boundary, ↓: upper boundary), while there is horizontal smearing that makes them up to three times as wide as they actually are. However, these effects are far less pronounced in the result obtained with workflow W1 (Fig. 10 (top)). Furthermore, the comparison of the resolution tests shows the significant increase in vertical resolution achieved by anisotropic gradient smoothing in the upper frequency stages of W1. When using workflow W2, the three shallow anomalies cause a high-velocity zone that dips toward the west (↙), similar to the observation from the field data using workflow W2, though with less merging. In the regions west and east of the high-velocity zone, the velocities are mostly decreased. The deep anomaly yields both a concave and a convex high-velocity zone at its western side (↙ and ↖). This effect does not occur when workflow W1 is used.

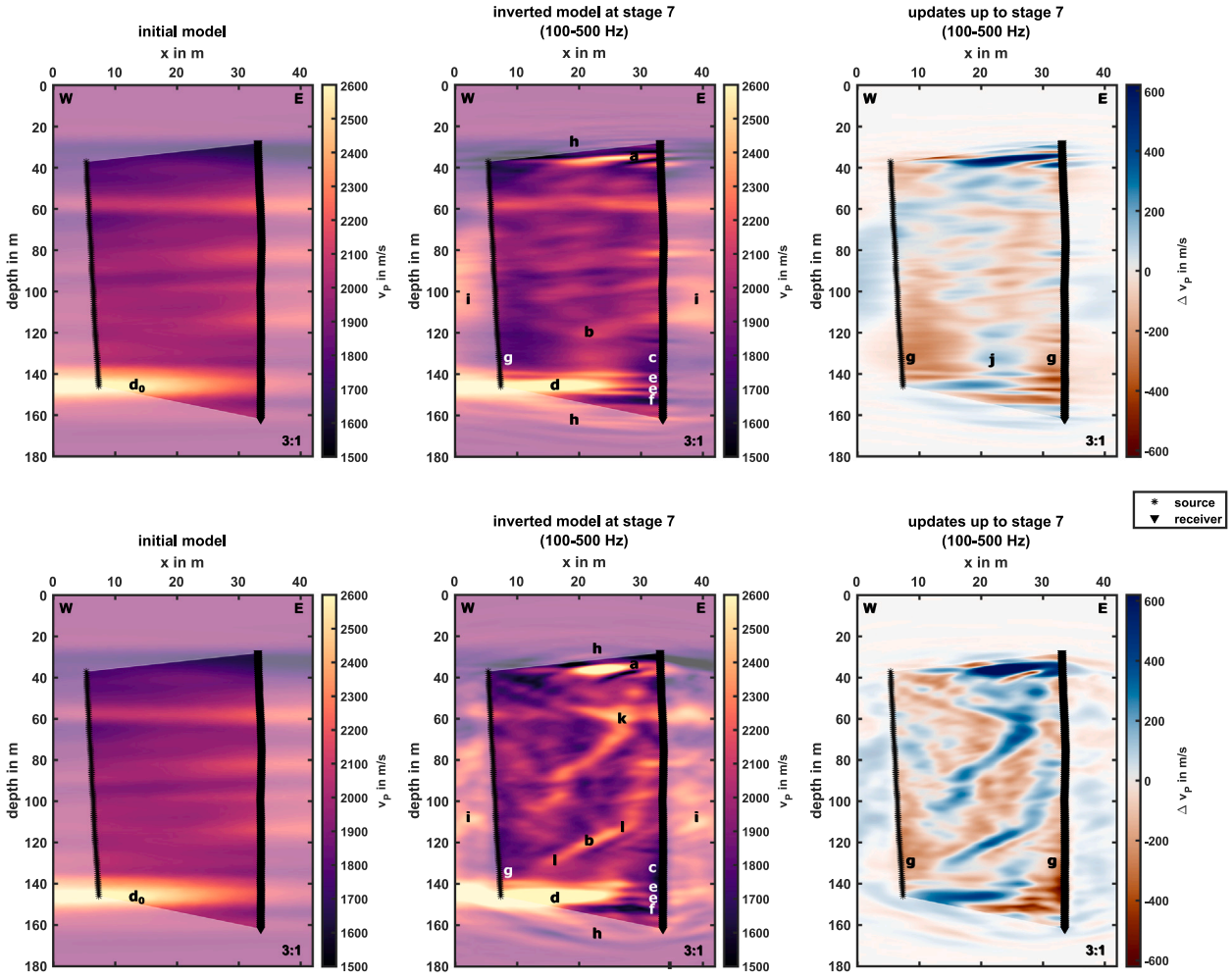

Fig. 6. Left: Traveltime tomography model, center: FWI result at stage 7 using workflow W1 (top) and workflow W2 (bottom), and right: difference between initial and inverted models at stage 7. Source positions are marked by stars (∗), receiver positions by triangles (▼). The unshaded areas in the model indicate areas of dense wavefield coverage. The labels a to e mark the velocity anomalies discussed in Section 6.1: (a) thin high-velocity layer, (b) depression, (c) alternating low-velocity layers, (d) very high-velocity layer, (d_0) high-velocity layer in FATT, (e) two low-velocity layers swerving from (d), (f) low-velocity layer, (g) low-velocity zone, (h) bending velocity zones, (i) model updates in boundaries, (j) increased velocities in central part of illuminated area, (k) X-shaped high-velocity zone, (l) slanted high-velocity zone tangential to depression (b).

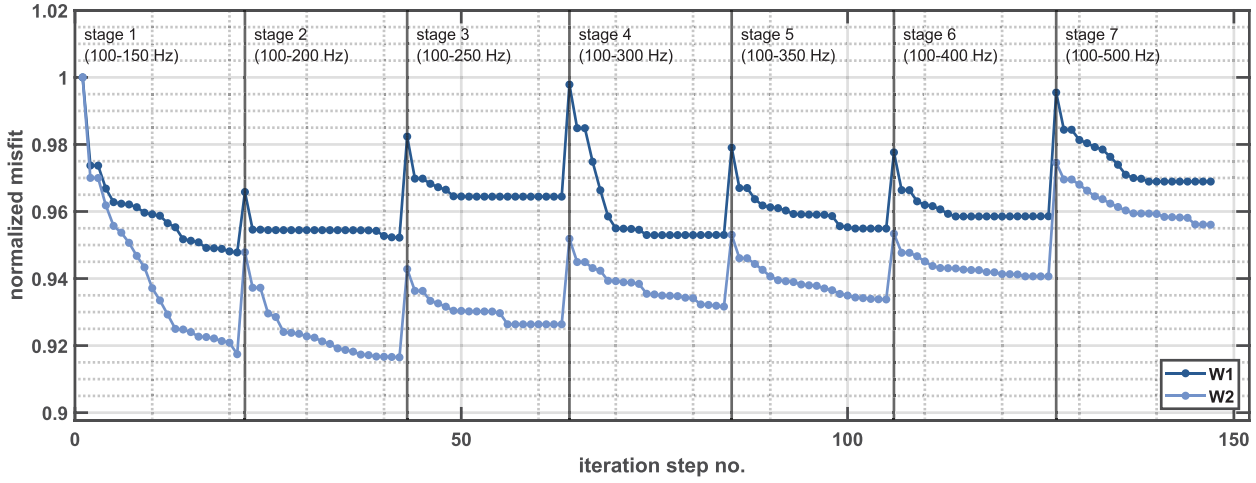

Fig. 7. Misfit evolution during the FWI normalized to initial misfit. The frequency content of the inversion stages is provided and the first iteration step at the new stages is marked by vertical lines.

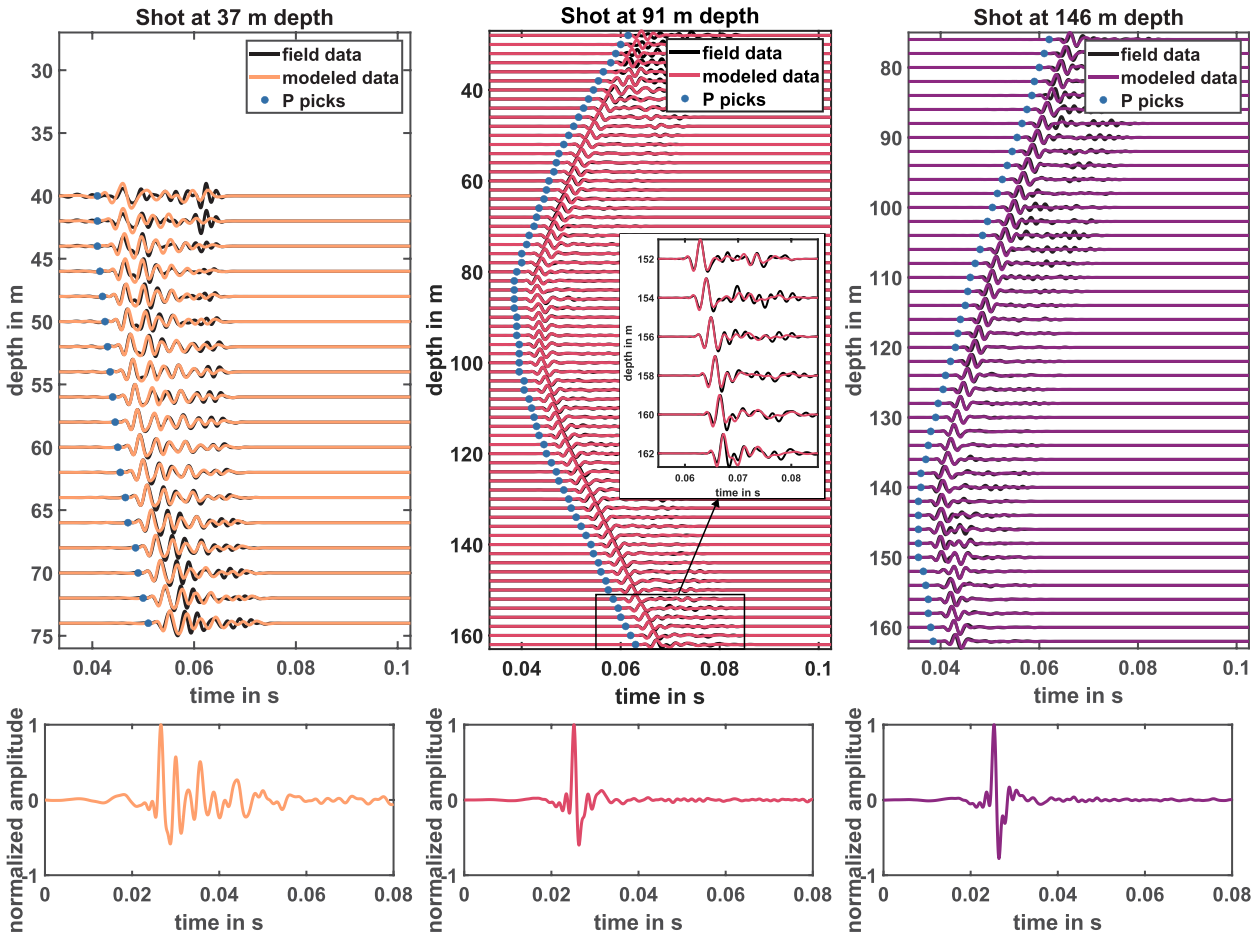

Fig. 8. Top: Waveform fit for the model at stage 7 (100–500 Hz) of the FWI using workflow W1 (Fig. 6) with the traveltime tomography models in Fig. 3 used as starting models. For better visualization, only every second trace is plotted, and an inset of the intermediate-depth shot presents an enlarged view of the deeper traces. Bottom: Normalized wavelets obtained by STF inversion using the stabilized Wiener deconvolution.

6.3. Comparison with sonic logs

Comparing velocity profiles, extracted from the models along the boreholes for the source and receiver positions, with the sonic wireline logging (Fig. 11), we observe that the FWI is closer to the sonic log at the source side of borehole B than at the receiver side of borehole C. Between 55 and 60 m depth, both workflows further increase the velocities along borehole C, which were already outside the sonic error range for the traveltime tomography model (FATT). Along borehole B, the velocities are also increased, but they stay within the sonic error range. Between 115 to 135 m depth, the FWI successfully reduces the velocities, where the FATT suggests higher velocities. While the velocity profile along borehole B lies within the sonic error range, the profile along borehole C shows an even greater velocity reduction, outside the sonic error range, below 130 m depth. Along borehole C, both FWI runs also introduce a negative velocity spike at about 124 m depth. In addition, the FWI velocity profiles are less smooth in this depth range than the sonic, which was smoothed using a Gaussian filter length that corresponds to its vertical resolution. While the seismic inversion runs show a smoothed version of the sonic for depths below 135 m along borehole B, the FWI results indicate more layering, including an interlayered low-velocity layer, where the sonic shows a thick high-velocity zone. Overall, the FWI velocities are slower than the sonic below 135 m along borehole C. Furthermore, the FWI runs reconstruct high-velocity layers above 40 m along borehole C, where no sonic information is available.

6.4. Correlation with lithology & 2D extrapolation

Our results show that the two FWI approaches yield similar velocity profiles along the boreholes (Fig. 11) but significant differences in the 2D borehole plane (Fig. 6) with workflow W2 resulting in stronger velocity contrasts and a more heterogeneous model.

A comparison with the final lithology derived from the core of borehole C is shown in Fig. 12. The FWI results reveal that the gravel exhibits a broad velocity distribution, including lower velocities at its base. However, these low velocities are considered less reliable due to the poor wavefield coverage above 37 m depth. High to very high velocities predominantly correlate with sand layers, particularly horizontally bedded sand (Sh).

The high-velocity layer just above 40 m depth (see also Fig. 6(a)), reconstructed using workflow W2, is especially prominent and appears to be shifted upward. In contrast, a similar layer reconstructed by workflow W1 aligns well with the uppermost sand layer, considering depth uncertainties and vertical resolution.

Similarly to the gravel, the diamict does not exhibit a distinct velocity range, but can mostly be distinguished in the velocity profiles from the surrounding material, e.g., at 60 m depth. An exception is the thin diamict layer just above 140 m depth, which is indistinguishable from the surrounding fines.

The fines tend to have intermediate (Fm, Fl, Fm(d), Fl(d)) to lower (Flr, Flr(d)) velocities. For further information on their properties, we refer to Schuster et al. (2024).

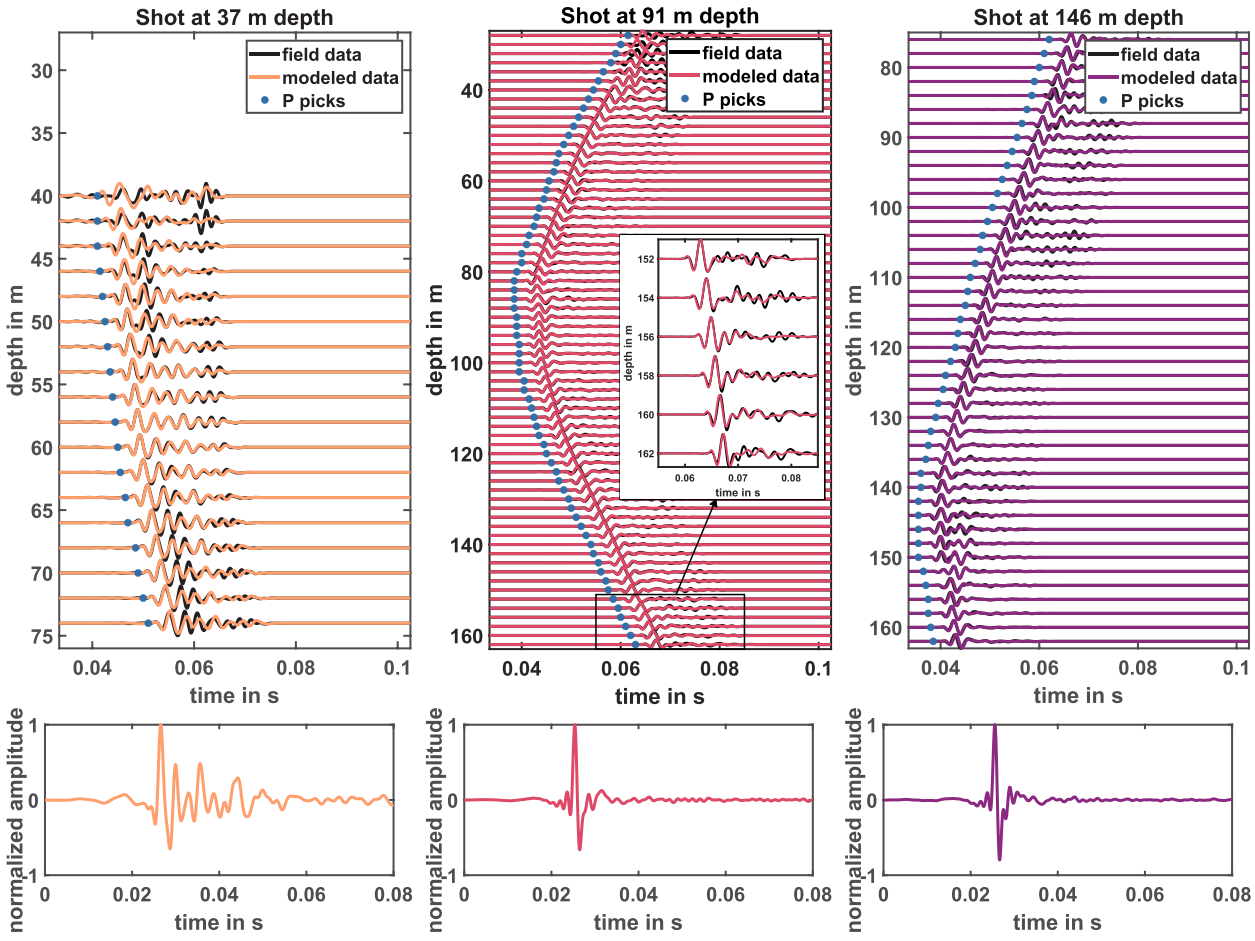

Fig. 9. Top: Waveform fit for the model at stage 7 (100–500 Hz) of the FWI using workflow W2 (Fig. 6) with the traveltime tomography models in Fig. 3 used as starting models. Noisy traces are muted and only every second trace is plotted for better visualization, and an inset of the intermediate-depth shot presents an enlarged view of the deeper traces. Bottom: Normalized wavelets obtained by STF inversion using the stabilized Wiener deconvolution.

The molasse bedrock (B) shows elevated P-wave velocities, though not as high as expected based on the sonic logs (Fig. 11).

Extrapolating this correlation to the 2D plane between boreholes B and C, we can infer a conceptual geological model by combining the two FWI results (Fig. 13, center), as each highlights different subsurface features according to its respective workflow focus. We interpret the high-velocity anomalies as sand packages. Furthermore, the model inverted by workflow W2 suggests a much more heterogeneous medium, reflecting a dynamic depositional environment. This is indicated by the colorgradient in some parts of the conceptual model. Due to the wavefield coverage, the interpretation will focus on depths below the shallowest receiver depth of 28 m.

The well-sorted, massive, and stratified sands (Sh, Sc) are weakly consolidated and show steep bedding in the deeper parts, according to Schuster et al. (2024). These sands are interpreted as glaciodeltaic deposits formed from the retreating glacier front during deglaciation (Buechi et al., 2018).

The depression at around 120 m depth is likely filled with massive, fine-grained deposits (Fm) and partly laminated sand (Sl) with a sandy or compacted layer at its base. It may have formed from either gravitational slumping of the sediments on the depositional slopes of the basin or from the glacier's load during an advance, as proposed by Schuster et al. (2024). The sand in the core was linked to hyper-concentrated density flow deposits (Mulder and Alexander, 2001; Schuster et al., 2024) and the filling of subaqueous channels (Sh) (Schuster et al., 2024; Beraus et al., 2025).

The interlayered low-velocity zones between the very high-velocity layers near the base, correlating with the bedrock, suggest that the drilling of borehole C may have hit molasse slabs, whereas at borehole B (Fig. 13(d)), the intact, massive molasse was reached.

7. Discussion

In a previous SV-wave study (Beraus et al., 2025), we attributed the lack of a depression at 120 m depth in the P-wave tomography model to the different material properties sampled by P- and S-waves. The present study, however, demonstrates the limitations of the acoustic first-arrival traveltime tomography in resolving this structure, while the high-resolution FWI is capable of delineating its shape to a certain extent (Fig. 6).

The steeply dipping high-velocity structures in the FWI results, most prominent in the result associated with workflow W2 (Fig. 6, bottom), are not geologically reasonable. The resolution test (Fig. 10) confirms that the X-shaped (k) and steeply dipping high-velocity features (l) are in fact the typical artifacts and their superposition in conjunction with denser sampling of the subsurface in high-velocities zones due to Fermat's principle. Furthermore, we have shown that they can be significantly reduced using anisotropic gradient smoothing (W1). Based on the outcome of the resolution test (Fig. 10), we hypothesize that the anomalies are not circular but more elliptical with a long axis that is oriented close to vertical. Furthermore, the velocity anomalies seem to have even higher velocities than the 2800 m s^{-1} used in the resolution test. The reconstruction attempt of the deep anomaly shows that a single anomaly at the apex of the depression (d) does not yield the steeply dipping feature (l) that is inverted with workflow W2. Therefore, we expect that there are several high-velocity anomalies

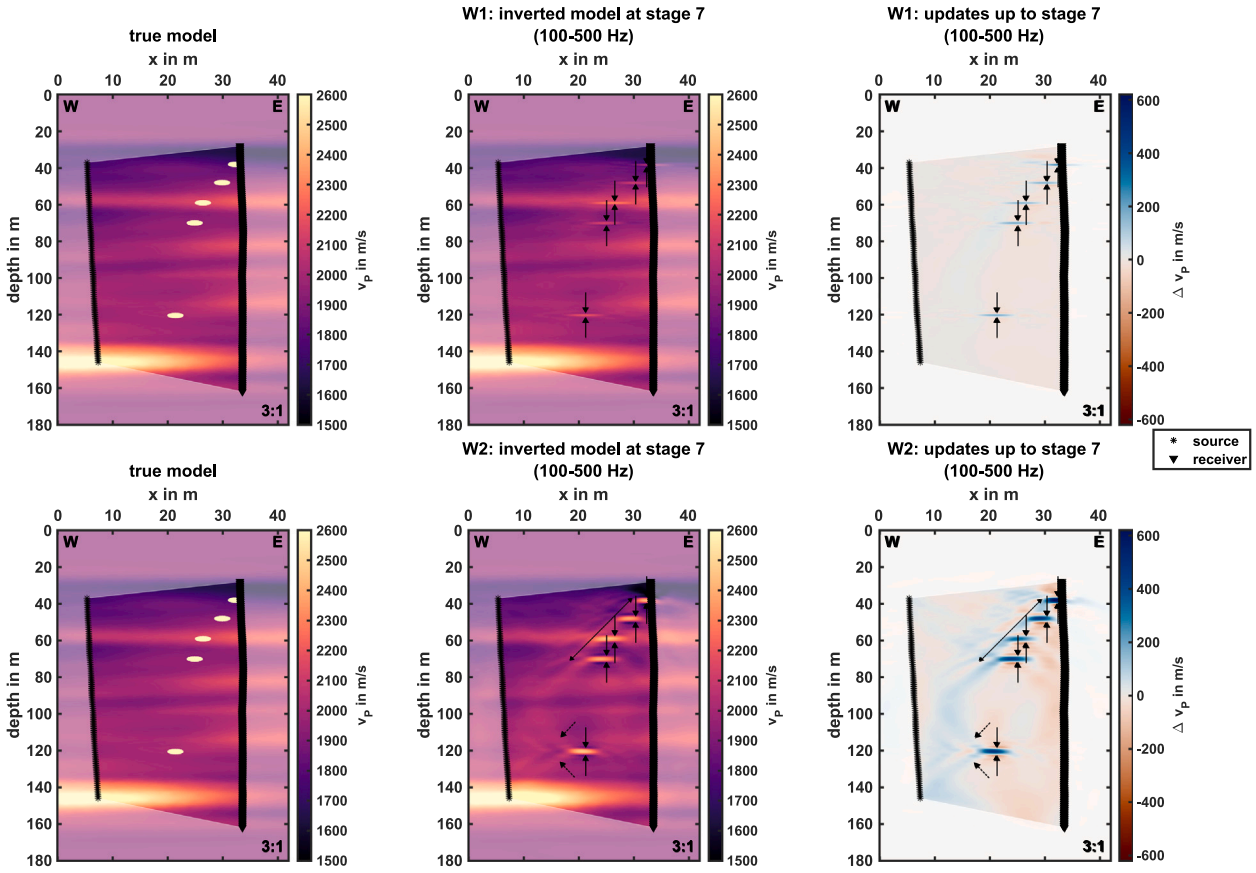

Fig. 10. Synthetic resolution tests using the traveltime tomography models including high-velocity anomalies and the two workflows. Source positions are marked by stars (*), receiver positions by triangles (▼). The unshaded areas in the model indicate areas of dense wavefield coverage. Left: True model consisting of the FATT model and circular high-velocity zones of 2800 m s^{-1}, where anomalies are expected to be located in the subsurface based on the field data FWI result of W1. Center: Inverted model at stage 7, and right: difference between initial and inverted model at stage 7. Top: The results using workflow 1 show almost no artifacts and a high vertical resolution. Bottom: Using workflow W2, significant artifacts appear. The three shallow reconstructed anomalies show sharper upper and lower boundaries (↑: lower boundary, ↓: upper boundary) than in the field data inversion result, but still form a steeply-dipping high-velocity zone west of the anomalies (↗); the single deep anomaly does not but yields both a concave and a convex high-velocity zone at its western side (↙ and ↙).

along the eastern flank of the depression (Fig. 13, center). Afanasiev et al. (2014) attribute these artifacts to a remaining mismatch between synthetic and observed waveforms at large offsets.

The wavelets (Figs. 5, 8 and 9) are derived from shot gathers composed of multiple receiver layouts, obtained using identical shot positions, though not necessarily with equivalent shot energy or coupling. Residual sparker and/or hydrophone motion from the previous shot will also influence the recorded waveforms. The remaining noise on some traces, particularly at the shallow shots, is most likely related to poor coupling due to gaps in the backfill between the PVC pipe and the gravel, and degrades the STF inversion result where it is coherent. Considering the waveform fit after FWI, it can be observed that small amplitude, incoherent later arrivals, although still included in the time-window, were not fitted by the inversion, whereas large amplitude reflections, such as the one at receiver depths around 150 m in the deepest shot, were fitted.

The velocity offset between the FATT and sonic logs along borehole C (Fig. 11) may stem from incorrect phase picking (trough vs. peak). Given the similarity in velocities between the sonic measurements in boreholes B and C, it is hypothesized that the crosshole picks, which were occasionally ambiguous due to temporal aliasing (Beraus et al., 2024b), could be further improved.

Traveltime tomography required intensive horizontal smoothing to converge (Beraus et al., 2024b). As this study shows, this assumption of horizontal continuity is not entirely valid for the infill of the glacially overdeepened basin. Nevertheless, the initial data fit attests to the suitability of the tomography model as initial model.

Furthermore, the requirement to strongly smooth the model horizontally to reduce artifacts may be an indicator that the physics used to describe the arrivals, e.g., isotropic wave propagation, may be insufficient. Hadden and Pratt (2017) have shown that anisotropic FWI applied to seismic data acquired in a sedimentary environment enhances the resolution and provides more accurate subsurface models. A prime candidate for anisotropy is the thick lithofacies assemblage (LFA) 4, as defined by Schuster et al. (2024), that consists of layered fines. The neglect of anisotropy may also contribute to the steeply dipping artifacts as observed by Hadden et al. (2019) who suggest an inaccurate characterization of the anisotropy. However, we expect the P-wave anisotropy of the glacial sediments to be small (von Ketelhodt et al., 2019) and superimposed by the complex heterogeneity of the sediments deposited in the glacially overdeepened basin.

The geological heterogeneity may similarly be considered in the workflow design of FWI, where we tested two reasonable definitions of gradient filters for the regularization of the inversion as it is suggested by Modrak and Tromp (2016). They and Wellington et al. (2019) have shown that gradient smoothing can significantly mitigate noise and spatial aliasing effects. According to them, gradient smoothing can also be used to introduce a priori information on the geology, e.g., strongest geological contrasts occurring vertically, into the inversion. Here we have shown, that while both workflows produce a similar final data fit, two very different velocity models are inverted. One that depicts the refined background velocity model with a very high vertical resolution (W1 using anisotropic gradient smoothing) and the other reveals local

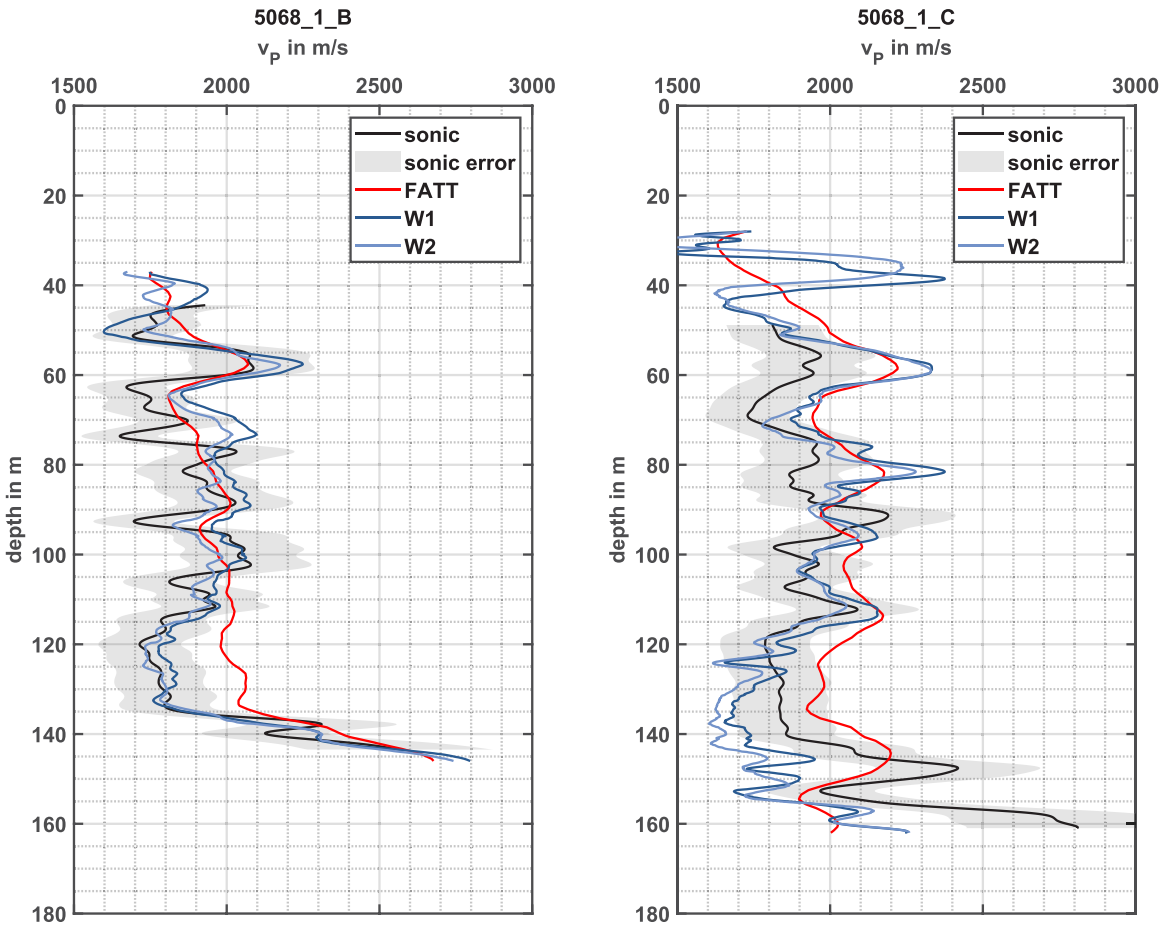

Fig. 11. Correlation of FWI profiles extracted along boreholes B and C from stage 7 (100–500 Hz) FWI models with sonic logs (DOVE-Phase 1 Scientific Team et al., 2023c,a), smoothed with a Gaussian filter of length 0.5 m (= d, see Section 5.4) and initial traveltime tomography (FATT) model.

high-velocity anomalies (W2 using isotropic gradient smoothing). Both of which are combined into a common conceptual geological sketch presented in Fig. 13. Using both workflows, targeting different geological features, to derive a comprehensive geological interpretation directly from the velocity models and the existing interpretation of core analysis (Schuster et al., 2024), allows to exploit the advantages of each, while discarding their respective disadvantages.

Regarding the correlation with the sonic logs (Fig. 11) to provide some ground-truthing, it has to be considered that the sonic logs only capture a few decimeters around the borehole – possibly disrupted by the drilling, especially in these soft sediments. Taking into account the thickness of the backfill and the estimated penetration depth, as determined by the mean velocity and sonic source frequency, we estimate that the illuminated volume surrounding the borehole is less than 20 cm in thickness. In contrast, the crosshole seismic samples about 28 m laterally. Nevertheless, using the sonics as constraints may help to guide the inversion (Wang and Rao, 2006). The trend towards decreasing velocities below 120 m depth at the receiver side along borehole C may be attributed to a reduced illumination intensity which is typically found on the periphery of the acquisition geometry and the boundary of the model.

Additionally, the circular gradient tapers that we applied around the source and receiver positions with a radius of 0.5 m, will also influence the absolute velocities in these areas and the model updates towards and in the boundary zones of the model.

Even though the correlation of the velocity profiles with the lithology from borehole C (Fig. 12) is satisfactory, slight shifts are observed. Apart from the depth location errors of sources and receivers in the acquisition due to cable extension (Beraus et al., 2024b), these may be related to the extension of the core at the surface due to the reduction of the surrounding pressure. This, besides the illumination deficiency, might also be, why the diamict at just above 140 m cannot be distinguished in the velocity profiles, which show slightly higher velocities at exactly 140 m depth. Alternatively, the thickness of the diamict is just outside the vertical resolution capability of both workflows.

8. Conclusions

Our seismic crosshole field data application of acoustic time-domain FWI shows the significant impact that the selected workflow has on the final velocity model. Therefore, we recommend systematically assessing numerous workflows, especially testing the gradient smoothing effect, and incorporating available a priori information. In case of a heterogeneous geology such as a glacially overdeepened basin, we find that using the FWI results of two workflows targeting extremal realizations of a glacially overdeepened geological setting is beneficial for inferring a comprehensive conceptual geological model by exploiting their respective advantages and mitigating their disadvantages. While anisotropic gradient smoothing (W1) yields what we interpret as a background model with high vertical resolution, isotropic gradient smoothing (W2) reveals local high-velocity anomalies.

This study further demonstrates that common criteria like (1) geological plausibility, (2) minimum data misfit, and (3) best correlation with other data, here sonic and core lithology, might not be sufficient to choose the optimal workflow.

Although a conceptual geological sketch can be inferred from the two FWI results, it is still a subjective result. Thus, we are convinced that it is necessary to include uncertainty quantification in FWI to assess

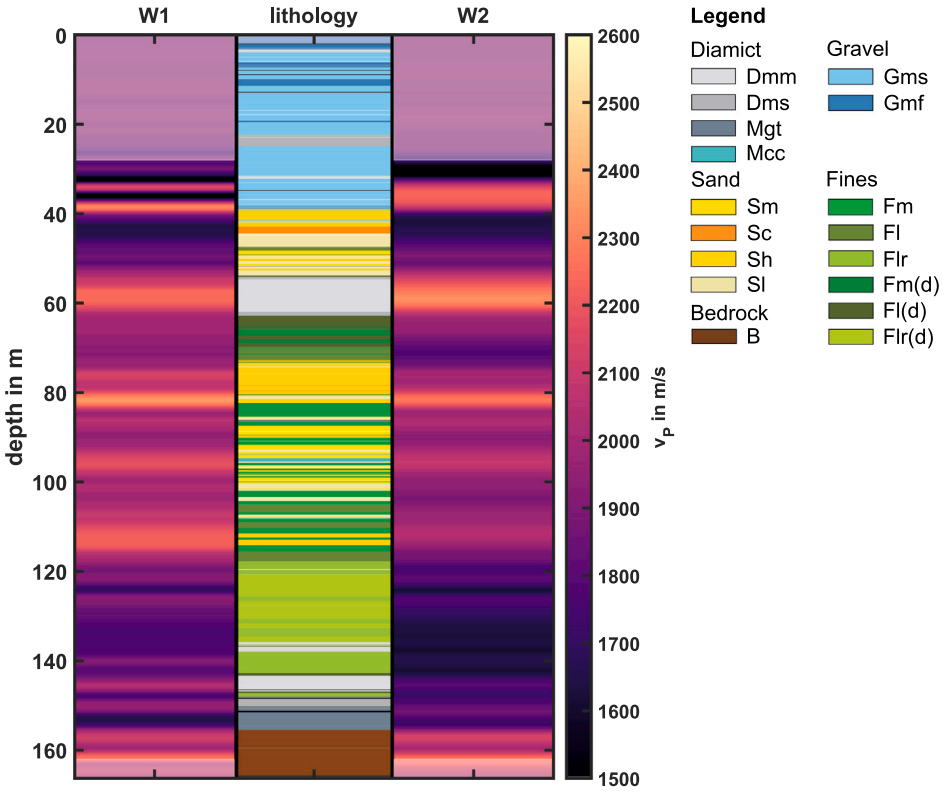

Fig. 12. Correlation of FWI results with the lithology that was retrieved from the core of borehole C. The shaded areas in the velocity profiles represent depths above and below the receiver locations. A detailed description of the facies codes can be found in Schuster et al. (2024) from which the legend was adapted from. (For interpretation of the references to color in this figure legend, the reader is referred to the web version of this article.)

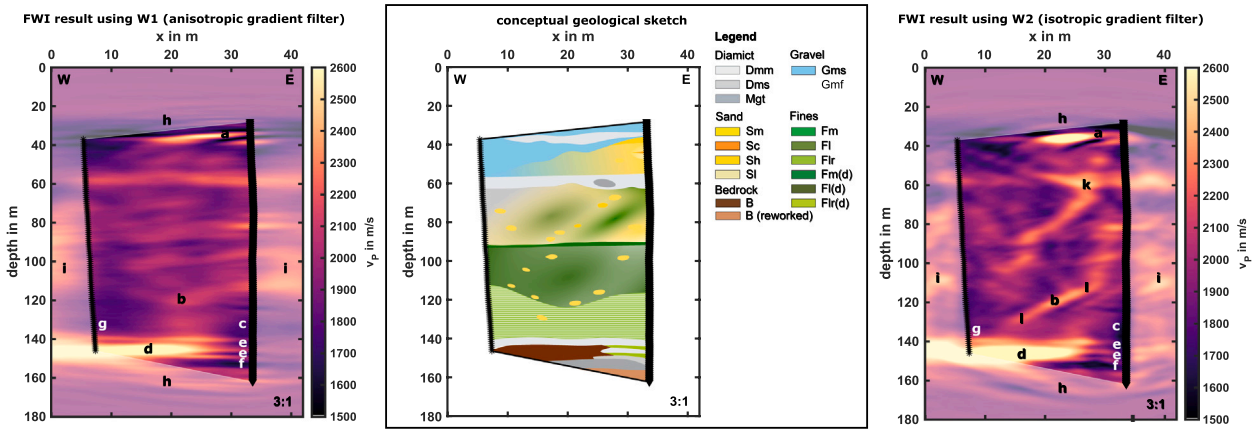

Fig. 13. Conceptual geological sketch (center) that combines the inversion results obtained by the two workflows (left and right). Source positions are marked by stars (*), receiver positions by triangles (▼). Colorgradients in the geological sketch indicate a heterogeneous medium. The striped green zone indicates thinly layered fines (c and g). The legend was adapted from Schuster et al. (2024), where a detailed description of the facies codes can be found. Note that, in case of fine scale heterogeneous velocities, the color representing the dominant material is used in the sketch. The labels in the FWI velocity models are introduced in Section 6.1. They identify to the following velocity features that are observed in the velocity models: (a) thin high-velocity layer, (b) depression, (c) alternating low-velocity layers, (d) very high-velocity layer, (e) two low-velocity layers swerving from (d), (f) low-velocity layer, (g) low-velocity zone, (h) bending velocity zones, (i) model updates in boundaries, (k) X-shaped high-velocity zone, (l) slanted high-velocity zone tangential to depression (b). (For interpretation of the references to color in this figure legend, the reader is referred to the web version of this article.)

the quality and geological plausibility of FWI results more reliably, independent of additional data, as traditional FWI alone cannot identify the best subsurface model using the three criteria listed above.

In addition, the velocity distribution alone provides only limited information for geological interpretation, such that we recommend including processing techniques like reflection seismics to obtain a structural image at the same resolution as FWI for a joint interpretation. Here, the high-resolution velocity model from FWI will ensure accurate structural migration.

CRediT authorship contribution statement

Sarah Beraus: Writing – review & editing, Writing – original draft, Visualization, Investigation, Formal analysis, Data curation, Conceptualization. **Daniel Köhn:** Writing – review & editing, Supervision, Software, Methodology, Investigation, Funding acquisition, Conceptualization. **Thomas Bohlen:** Writing – review & editing, Supervision, Software, Methodology. **Thomas Burschil:** Funding acquisition, Conceptualization. **Hermann Buness:** Funding acquisition, Data curation, Conceptualization. **Gerald Gabriel:** Writing – review & editing, Supervision, Project administration.

Financial support

This research has been funded by Deutsche Forschungsgemeinschaft, Germany (grants: BU 3894/2-1, BU 2467/3-1 and KO 6375/1-1) within the priority program 1006 (ICDP).

Declaration of competing interest

The authors declare that they have no known competing financial interests or personal relationships that could have appeared to influence the work reported in this paper.

Acknowledgments

We acknowledge the International Continental Drilling Program (ICDP) for their continued support and funding for the drilling of the three boreholes at ICDP site 5068_1. Furthermore, we thank the reviewers for their constructive feedback, which helped improve the clarity and quality of the manuscript. The seismic crosshole equipment was rented from Geotomographie GmbH, Neuwied, Germany. A special thanks to the technical staff of LIAG-FA11 Jan Bayerle, Sven Wedig and Jan Bergmann Barrocas as well as our student assistant Kim Ripke for their vigorous support in the field. Many thanks to Thomas Grelle and Carlos Lehne of LIAG-FA22 for acquiring the wireline logging data, and Thomas Wonik for preparing the data for the DOVE project and providing explanations. Additional thanks goes to the Applied Geophysics working group at KIT for helpful discussions about FWI and the DOVE group for valuable insights into the geology of overdeepened basins. Preprocessing of the data was done using an academic license of Shearwater's Reveal software and the open-source code BIRGIT. FWI was performed on the NEC-HPC Linux-Cluster at Kiel University and the GWDG SSC Cluster in Göttingen using the DENISE-Black Edition code. The authors acknowledge the IT department of LIAG for organizing and supporting access to the GWDG SSC Cluster. Last but not least, we thank the editor and the anonymous reviewers of the manuscript.

Data availability

Upon completion of the project, the seismic data is accessible via GFZ data services (https://doi.org/10.5880/ICDP.5068.002, Beraus et al. (2024a).

References

Afanasiev, M.V., Pratt, R.G., Kamei, R., McDowell, G., 2014. Waveform-based simulated annealing of crosshole transmission data: a semi-global method for estimating seismic anisotropy. Geophys. J. Int. 199 (3), 1586–1607. http://dx.doi.org/10.1093/gji/ggu307.

Alford, R.M., Kelly, K.R., Boore, D.M., 1974. Accuracy of finite-difference modeling of the acoustic wave equation. Geophysics 39 (6), 834–842. http://dx.doi.org/10.1190/1.1440470.

Barnes, C., Charara, M., Tsuchiya, T., 2008. Feasibility study for an anisotropic full waveform inversion of cross-well seismic data. Geophys. Prospect. 56 (6), 897–906. http://dx.doi.org/10.1111/j.1365-2478.2008.00702.x.

Beraus, S., Buness, H., Bayerle, J., Bergmann Barrocas, J., Wedig, S., Ripke, K., Gabriel, G., 2024a. Crosshole seismic data at ICDP site 5068_1 [dataset]. http://dx.doi.org/10.5880/ICDP.5068.002.

Beraus, S., Burschil, T., Buness, H., Köhn, D., Bohlen, T., Gabriel, G., 2024b. A comprehensive crosshole seismic experiment in glacial sediments at the ICDP DOVE site in the Tannwald Basin. Sci. Drill. 33 (2), 237–248. http://dx.doi.org/10.5194/sd-33-237-2024.

Beraus, S., Köhn, D., Bohlen, T., Burschil, T., Schuster, B., Buness, H., Gabriel, G., 2025. Seismic crosshole full-waveform inversion of high-frequency SV-waves for glacial sediment characterization. Geophys. Prospect. 73 (5), 1587–1605. http://dx.doi.org/10.1111/1365-2478.70024.

Bleistein, N., 1986. Two-and-One-Half dimensional in-plane wave propagation. Geophys. Prospect. 34 (5), 686–703. http://dx.doi.org/10.1111/j.1365-2478.1986.tb00488.x.

Buechi, M.W., Graf, H.R., Haldimann, P., Lowick, S.E., Anselmetti, F.S., 2018. Multiple Quaternary erosion and infill cycles in overdeepened basins of the northern Alpine foreland. Swiss J. Geosci. 111 (1), 133–167. http://dx.doi.org/10.1007/s00015-017-0289-9.

Buness, H., Tanner, D.C., Burschil, T., Gabriel, G., Wielandt-Schuster, U., 2022. Cuspate-lobate folding in glacial sediments revealed by a small-scale 3-D seismic survey. J. Appl. Geophys. 200, 104614. http://dx.doi.org/10.1016/j.jappgeo.2022.104614.

Bunks, C., Saleck, F., Zaleski, S., Chavent, G., 1995. Multiscale seismic Wave-Form inversion. Geophysics 60, 1457–1473. http://dx.doi.org/10.1190/1.1443880.

Burschil, T., Buness, H., Tanner, D., Wielandt-Schuster, U., Ellwanger, D., Gabriel, G., 2018. High-resolution reflection seismics reveal the structure and the evolution of the Quaternary glacial Tannwald Basin. Near Surf. Geophys. 16, 593–610. http://dx.doi.org/10.1002/nsg.12011.

Choi, Y., Alkhalifah, T., 2012. Application of multi-source waveform inversion to marine streamer data using the global correlation norm. Geophys. Prospect. 60 (4), 748–758. http://dx.doi.org/10.1111/j.1365-2478.2012.01079.x.

Cook, S., Swift, D., 2012. Subglacial basins: Their origin and importance in glacial systems and landscapes. Earth-Sci. Rev. 115, 332–372. http://dx.doi.org/10.1016/j.earscirev.2012.09.009.

Courant, R., Friedrichs, K., Lewy, H., 1967. On the partial difference equations of mathematical physics. IBM J. Res. Dev. 11 (2), 215–234. http://dx.doi.org/10.1147/rd.112.0215.

Crameri, F., 2023. Scientific colour maps. http://dx.doi.org/10.5281/zenodo.8409685, URL: https://zenodo.org/records/8409685.

Dablain, M.A., 1986. The application of high-order differencing to the scalar wave equation. Geophysics 51 (1), 54–66. http://dx.doi.org/10.1190/1.1442040.

DOVE-Phase 1 Scientific Team, Anselmetti, F.S., Beraus, S., Buechi, M., Buness, H., Burschil, T., Fiebig, M., Firla, G., Gabriel, G., Gegg, L., Grelle, T., Heeschen, K., Kroemer, E., Lehne, C., Lüthgens, C., Neuhuber, S., Preusser, F., Schaller, S., Schmalfuss, C., Schuster, B., Tanner, D.C., Thomas, C., Tomonaga, Y., Wieland-Schuster, U., Wonik, T., 2023a. Drilling overdeepened alpine valleys (DOVE) - Operational dataset of DOVE phase 1. http://dx.doi.org/10.5880/ICDP.5068.001, Publisher: GFZ German Research Centre for Geosciences.

DOVE-Phase 1 Scientific Team, F.S., Beraus, S., Buechi, M.W., Buness, H., Burschil, T., Fiebig, M., Firla, G., Gabriel, G., Gegg, L., Grelle, T., Heeschen, K., Kroemer, E., Lehne, C., Lüthgens, C., Neuhuber, S., Preusser, F., Schaller, S., Schmalfuss, C., Schuster, B., Tanner, D.C., Thomas, C., Tomonaga, Y., Wieland-Schuster, U., Wonik, T., 2023b. Drilling overdeepened alpine valleys (DOVE) - Explanatory remarks on the operational dataset. http://dx.doi.org/10.48440/ICDP.5068.002, Publisher: GFZ German Research Centre for Geosciences.

DOVE-Phase 1 Scientific Team, F.S., Beraus, S., Buechi, M.W., Buness, H., Burschil, T., Fiebig, M., Firla, G., Gabriel, G., Gegg, L., Grelle, T., Heeschen, K., Kroemer, E., Lehne, C., Lüthgens, C., Neuhuber, S., Preusser, F., Schaller, S., Schmalfuss, C., Schuster, B., Tanner, D.C., Thomas, C., Tomonaga, Y., Wieland-Schuster, U., Wonik, T., 2023c. Drilling Overdeepened Alpine Valleys (DOVE) – Operational Report of Phase 1. ICDP Operational Report, http://dx.doi.org/10.48440/ICDP.5068.001, Publisher: GFZ German Research Centre for Geosciences.

Ellwanger, D., Lämmermann-Barthel, J., Neeb, I., 2003. Eine landschaftsübergreifende Lockergesteinsgliederung vom Alpenrand zum Oberrhein. GeoArchaeoRhein 4, 81–124.

Ellwanger, D., Wielandt-Schuster, U., Franz, M., Simon, T., 2011. The Quaternary of the southwest German Alpine foreland (Bodensee, Oberschwaben, Baden- Württemberg, Southwest Germany). Quat. Sci. J. 0424-7116 60, 306–328. http://dx.doi.org/10.3285/eg.60.2-3.07.

Forbriger, T., Groos, L., Schäfer, M., 2014. Line-source simulation for shallow-seismic data. Part 1: theoretical background. Geophys. J. Int. 198 (3), 1387–1404. http://dx.doi.org/10.1093/gji/ggu199.

Gardner, G.H.F., Gardner, L.W., Gregory, A.R., 1974. Formation velocity and density—the diagnostic basics for stratigraphic traps. Geophysics 39 (6), 770–780. http://dx.doi.org/10.1190/1.1440465.

Günther, T., Rücker, C., Spitzer, K., 2006. Three-dimensional modelling and inversion of dc resistivity data incorporating topography — II. Inversion. Geophys. J. Int. 166 (2), 506–517. http://dx.doi.org/10.1111/j.1365-246X.2006.03011.x.

Hadden, S., Pratt, R., 2017. Full waveform inversion of crosshole data in tilted transversely isotropic media. In: 79th EAGE Conference and Exhibition 2017. Vol. 2017, European Association of Geoscientists & Engineers, pp. 1–5. http://dx.doi.org/10.3997/2214-4609.201700793.

Hadden, S., Pratt, R.G., Smithyman, B., 2019. Anisotropic full-waveform inversion of crosshole seismic data: A vertical symmetry axis field data application. Geophysics 84 (1), B15–B32. http://dx.doi.org/10.1190/geo2017-0790.1.

Jordi, C., Doetsch, J., Günther, T., Schmelzbach, C., Robertsson, J.O., 2018. Geostatistical regularization operators for geophysical inverse problems on irregular meshes. Geophys. J. Int. 213 (2), 1374–1386. http://dx.doi.org/10.1093/gji/ggy055.

Köhn, D., 2025a. BIRGIT [software]. URL: https://github.com/daniel-koehn/BIRGIT, original-date: 2019-01-16T02:25:26Z.

Köhn, D., 2025b. DENISE-black-edition [software]. URL: https://github.com/daniel-koehn/DENISE-Black-Edition, original-date: 2015-03-28T02:40:38Z.

Köhn, D., De Nil, D., Kurzmann, A., Przebindowska, A., Bohlen, T., 2012. On the influence of model parametrization in elastic full waveform tomography. Geophys. J. Int. 191 (1), 325–345. http://dx.doi.org/10.1111/j.1365-246X.2012.05633.x.

Komatitsch, D., Martin, R., 2007. An unsplit convolutional Perfectly Matched Layer improved at grazing incidence for the seismic wave equation. Geophysics 72, SM155–SM167. http://dx.doi.org/10.1190/1.2757586.

Kühn, F., 2018. Ultrasound Medical Imaging Using 2d Viscoacoustic Full-Waveform Inversion (Master's thesis). Karlsruher Institut für Technologie (KIT), http://dx.doi.org/10.5445/IR/1000089567.

Kurzmann, A., 2012. Applications of 2D and 3D Full Waveform Tomography in Acoustic and Viscoacoustic Complex Media (Ph.D. thesis). Karlsruher Institut für Technologie (KIT), http://dx.doi.org/10.5445/IR/1000034421.

Levander, A., 1988. Fourth-order finite-difference P-S. Geophysics 53, 1425–1436. http://dx.doi.org/10.1190/1.1442422.

Mecking, R., Köhn, D., Meinecke, M., Rabbel, W., 2021. Cavity detection by SH-wave full-waveform inversion — A reflection-focused approach. Geophysics 86 (3), WA123–WA137. http://dx.doi.org/10.1190/geo2020-0349.1.

Modrak, R., Tromp, J., 2016. Seismic waveform inversion best practices: regional, global and exploration test cases. Geophys. J. Int. 206 (3), 1864–1889. http://dx.doi.org/10.1093/gji/ggw202.

Mulder, T., Alexander, J., 2001. The physical character of subaqueous sedimentary density flows and their deposits. Sedimentology 48 (2), 269–299. http://dx.doi.org/10.1046/j.1365-3091.2001.00360.x.

Nocedal, J., Wright, S., 2006. Numerical Optimization. Springer Science+Business Media, LLC, New York, NY, http://dx.doi.org/10.1007/978-0-387-40065-5.

Polak, E., Ribiere, G., 1969. Note sur la convergence de méthodes de directions conjuguées. Rev. Française D'Inform. Rech. Opér. Sér. Rouge 3, 35–43, URL: http://www.numdam.org/item/?id=M2AN_1969__3_1_35_0.

Pratt, R., Hou, F., Bauer, K., Weber, M., 2005. Waveform tomography images of velocity and inelastic attenuation from the Mallik 2002 crosshole seismic surveys. In: S.R. Dallimore, T.C. (Ed.), Scientific Results from the Mallik 2002 Gas Hydrate Production Research Well Program, Mackenzie Delta, Northwest Territories, Canada. In: GSC Bulletin, Vol. 585, Geological Survey of Canada, URL: https://eurekamag.com/research/024/128/024128777.php.

Pratt, R., Shipp, R., 1999. Seismic waveform inversion in the frequency domain, Part 2: Fault delineation in sediments using crosshole data. Geophysics 64 (3), 902–914. http://dx.doi.org/10.1190/1.1444598.

Preusser, F., Reitner, J.M., Schlüchter, C., 2010. Distribution, geometry, age and origin of overdeepened valleys and basins in the Alps and their foreland. Swiss J. Geosci. 103 (3), 407–426. http://dx.doi.org/10.1007/s00015-010-0044-y.

Ravaut, C., Operto, S., Improta, L., Virieux, J., Herrero, A., Dell'Aversana, P., 2004. Multiscale imaging of complex structures from multifold wide-aperture seismic data by frequency-domain full-waveform tomography: Application to a thrust belt. Geophys. J. Int. 159, 1032–1056. http://dx.doi.org/10.1111/j.1365-246X.2004.02442.x.

Rücker, C., Günther, T., Wagner, F.M., 2017. pyGIMLi: An open-source library for modelling and inversion in geophysics. Comput. Geosci. 109, 106–123. http://dx.doi.org/10.1016/j.cageo.2017.07.011.

Schäfer, M., Groos, L., Forbriger, T., Bohlen, T., 2014. Line-source simulation for shallow-seismic data. Part 2: full-waveform inversion—a synthetic 2-D case study. Geophys. J. Int. 198 (3), 1405–1418. http://dx.doi.org/10.1093/gji/ggu171.

Schaller, S., Becerra, P., Beraus, S., Buechi, M.W., Mair, D., Abadi, M.S., Schuster, B., Anselmetti, F.S., 2025. Data-driven lithofacies prediction of unconsolidated sediments from wireline logs. Sedimentologika 3 (1), 1–18. http://dx.doi.org/10.57035/journals/sdk.2025.e31.1819.

Schuster, B., Gegg, L., Schaller, S., Buechi, M.W., Tanner, D.C., Wielandt-Schuster, U., Anselmetti, F.S., Preusser, F., 2024. Shaped and filled by the Rhine Glacier: the overdeepened Tannwald Basin in southwestern Germany. Sci. Drill. 33 (2), 191–206. http://dx.doi.org/10.5194/sd-33-191-2024.

Schwardt, M., Köhn, D., Wunderlich, T., Wilken, D., Seeliger, M., Schmidts, T., Brückner, H., Başaran, S., Rabbel, W., 2020. Characterization of silty to fine-sandy sediments with SH waves: full waveform inversion in comparison with other geophysical methods. Near Surf. Geophys. 18 (3), 217–248. http://dx.doi.org/10.1002/nsg.12097.

Tarantola, A., 1984. Linearized inversion of seismic reflection data*. Geophys. Prospect. 32 (6), 998–1015. http://dx.doi.org/10.1111/j.1365-2478.1984.tb00751.x.

Tromp, J., 2020. Seismic wavefield imaging of Earth's interior across scales. Nat. Rev. Earth Environ. 1 (1), 40–53. http://dx.doi.org/10.1038/s43017-019-0003-8.

Virieux, J., Operto, S., 2009. An overview of full-waveform inversion in exploration geophysics. Geophysics 74 (6), WCC1–WCC26. http://dx.doi.org/10.1190/1.3238367.

von Ketelhodt, J., Manzi, M., Durrheim, R., Fechner, T., 2019. Seismic VTI parameter inversion from P- and S-wave Cross-Borehole measurements in an aquifer environment. Geophysics 84, 1–57. http://dx.doi.org/10.1190/geo2018-0335.1.

Wang, Y., Rao, Y., 2006. Crosshole seismic waveform tomography – I. Strategy for real data application. Geophys. J. Int. 166 (3), 1224–1236. http://dx.doi.org/10.1111/j.1365-246X.2006.03030.x.

Warner, M., Ratcliffe, A., Nangoo, T., Morgan, J., Umpleby, A., Shah, N., Vinje, V., Štekl, I., Guasch, L., Win, C., Conroy, G., Bertrand, A., 2013. Anisotropic 3D full-waveform inversion. Geophysics 78 (2), R59–R80. http://dx.doi.org/10.1190/geo2012-0338.1.

Watanabe, T., Shimizu, S., Asakawa, E., Kamei, R., Matsuoka, T., Watanabe, T., Shimizu, S., Asakawa, E., Kamei, R., Matsuoka, T., 2005. Preliminary assessment of the waveform inversion method for interpretation of cross-well seismic data from the thermal production test, JAPEX/ JNOC/ GSC et al. Mallik 5L-38 gas hydrate production research well. In: S.R. Dallimore, T.C. (Ed.), Scientific Results from the Mallik 2002 Gas Hydrate Production Research Well Program, Mackenzie Delta, Northwest Territories, Canada. In: GSC Bulletin, vol. 585, Geological Survey of Canada, URL: https://eurekamag.com/research/023/399/023399500.php.

Wellington, P., Brossier, R., Virieux, J., 2019. Preconditioning full-waveform inversion with efficient local correlation operators. Geophysics 84 (3), R321–R332. http://dx.doi.org/10.1190/geo2018-0584.1.

Yang, J., He, X., Wang, S., Chen, H., 2024. Monitoring underground hydrogen storage migration and distribution using time-lapse acoustic waveform inversion. Int. J. Hydrog. Energy 69, 272–281. http://dx.doi.org/10.1016/j.ijhydene.2024.05.002.

Yee, K., 1966. Numerical solution of initial boundary value problems involving maxwell's equations in isotropic media. IEEE Trans. Antennas and Propagation 14 (3), 302–307. http://dx.doi.org/10.1109/TAP.1966.1138693.

Zhang, F., Juhlin, C., Cosma, C., Tryggvason, A., Pratt, R.G., 2012. Cross-well seismic waveform tomography for monitoring CO2 injection: a case study from the Ketzin Site, Germany. Geophys. J. Int. 189 (1), 629–646. http://dx.doi.org/10.1111/j.1365-246X.2012.05375.x.

Zhou, C., Schuster, G.T., Hassanzadeh, S., Harris, J.M., 1997. Elastic wave equation traveltime and waveform inversion of crosswell data. Geophysics 62 (3), 853–868. http://dx.doi.org/10.1190/1.1444194.